Inorganic Chemistry

Local vs Nonlocal States in FeTiO$_3$ Probed with 1s2pRIXS: Implications for Photochemistry

Myrtille O. J. Y. Hunault,*,[†] Wilayat Khan,[‡] Jan Minár,[‡] Thomas Kroll,[§] Dimosthenis Sokaras,[§] Patric Zimmermann,[†] Mario U. Delgado-Jaime,[†] and Frank M. F. de Groot*,[†]
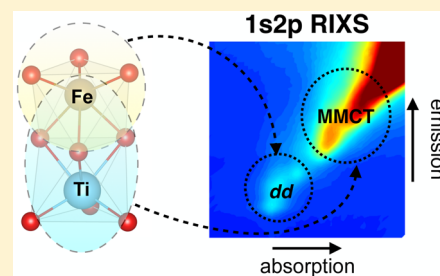
[†]Inorganic Chemistry and Catalysis, Debye Institute for Nanomaterial Science, Utrecht University, 3584CG Utrecht, The Netherlands

[‡]New Technologies-Research Center, University of West Bohemia, Univerzitni 8, 306 14 Plzeň, Czech Republic

[§]Stanford Synchrotron Radiation Lightsource (SSRL), SLAC National Accelerator Laboratory, Menlo Park, California 94025, United States

S *Supporting Information*

ABSTRACT: Metal−metal charge transfer (MMCT) is expected to be the main mechanism that enables the harvesting of solar light by iron−titanium oxides for photocatalysis. We have studied FeTiO$_3$ as a model compound for MMCT with 1s2pRIXS at the Fe K-edge. The high-energy resolution XANES enables distinguishing five pre-edge features. The three first well distinct RIXS features are assigned to electric quadrupole transitions to the localized Fe* 3d states, shifted to lower energy by the 1s core−hole. Crystal field multiplet calculations confirm the speciation of divalent iron. The contribution of electric dipole absorption due to local p-d mixing allowed by the trigonal distortion of the cation site is supported by DFT and CFM calculations. The two other nonlocal features are assigned to electric dipole transitions to excited Fe* 4p states mixed with the neighboring Ti 3d states. The comparison with DFT calculations demonstrates that MMCT in ilmenite is favored by the hybridization between the Fe 4p and delocalized Ti 3d orbitals via the O 2p orbitals.

INTRODUCTION

Hematite (α-Fe$_2$O$_3$) has been extensively considered for the development of photocatalysts as a low-cost and nontoxic material.[1] Various dopings have been investigated to improve its low charge-carrier transport properties and to optimize its optical absorption, among which Ti-doping appeared as a promising solution.[2] Alternatively, efficient Fe−Ti associations have also been considered in various oxides[3] including heterojunction assemblies of iron and titanium oxides,[4] in dye sensitized solar cells,[5] and in heterobinuclear complexes.[6] In all of these, the photoinduced metal−metal charge transfer (MMCT) is expected to be the main mechanism that enables harvesting solar light energy with multivalent transition metal ions in both solid state and molecular complexes.[7]

The present study focuses on ilmenite (FeTiO$_3$) as a model compound for the metal−metal charge transfer process in Ti-doped hematite. MMCT in FeTiO$_3$ has been first reported from optical absorption spectroscopy[8] by analogy with the optical absorption spectrum of blue sapphire (Fe- and Ti-doped Al$_2$O$_3$).[9] Like hematite, ilmenite has a corundum structure (space group $R\bar{3}$) in which Ti and Fe occupy alternating layers of octahedrons along the c axis of the hexagonal unit cell (Figure 1). As a result, the Fe and Ti neighboring octahedrons share a face. This particular linkage is expected to play a key role in the direct cation−cation interactions[10] and in particular to enable MMCT via the direct overlap of the Fe and Ti z^2
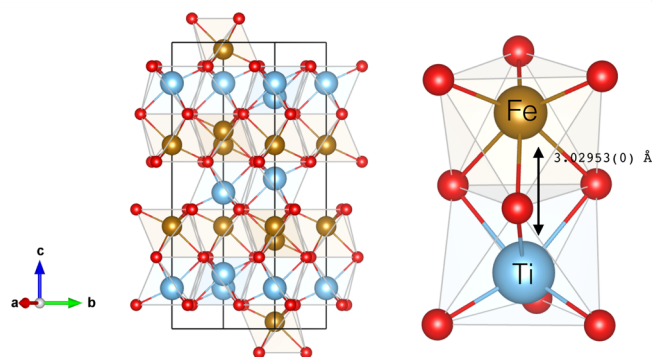

Figure 1. Crystal structure of ilmenite FeTiO$_3$ and zoom on the face sharing Fe and Ti octahedrons.

orbitals through the shared face. MMCT has also been observed with edge or corner bridged polyhedrons, in solids or heterobinuclear complexes, which questions the influence of the atomic structure and the nature of the anions in the MMCT efficiency.[6d,7a,11,12]

The valence states of iron and titanium cations in these compounds are also of great importance to determine the MMCT mechanism. While hematite is formally a high-spin

Fe^{3+} oxide, the valence states of iron and titanium in ilmenite are suggested to be high-spin Fe^{2+} and Ti^{4+} respectively. The intermetallic charge transfer implies the transfer of an electron from Fe to Ti: $Fe^{2+} + Ti^{4+} \rightarrow Fe^{3+} + Ti^{3+}$. High-pressure induced Fe^{2+} to Fe^{3+} valence changes have been reported from Mossbauer and X-ray absorption (XAS) spectroscopies.[13] Therefore, the determination of the exact valence states of the metal cations in the ilmenite motivated several spectroscopic studies at the $L_{2,3}$-edges of Ti and at the Ti and Fe $L_{2,3}$-edges and O K-edge. In an early resonant inelastic X-ray scattering (RIXS) study at the Ti $L_{2,3}$-edge, Butorin et al. suggested that low-energy optical excited states (ca. 4 eV) were due to Ti^{3+}.[14] Later, Radtke et al. confirmed using high-resolution electron energy loss spectroscopy (EELS) at the $L_{2,3}$-edges of Ti and Fe, their respective tetravalent and divalent oxidation states.[15] A second Ti $L_{2,3}$-edge RIXS study supported by Fe−Ti double cluster calculations assigned the low-energy excitations observed in RIXS around 2.5 and 4 eV to MMCT.[16]

In K-edge XAS, the weak $1s$ core−hole interaction with the valence electrons and the absence of orbital momentum of the s shell considerably decrease the influence of core−hole spin−orbit coupling compared to $L_{2,3}$-edge XAS.[17] Both electric dipole (E1) and electric quadrupole (E2) transitions can contribute to the pre-edge features at the onset of the K-edge. Their analysis allows one to derive useful information about the orbital hybridization of the absorbing cation. These pre-edge features arise from E2 transitions to $3d$ excited states splitted by multielectronic interactions and crystal field effects, and also E1 transitions to local and/or delocalized excited states with p character, which enhance the E2 pre-edge feature intensity and/or result in nonlocal features.[18−21] To our knowledge, only one study of the Ti and Fe K-edge X-ray absorption near-edge structure (XANES) in $FeTiO_3$ was reported so far.[22] O K-edge results have revealed the overlap between the Ti $3d$ and O $2p$ orbitals.[15,22] Despite these previous investigations, the particular role of oxygen and the contribution of Fe to the orbitals involved in the MMCT remains unclear and the picture of the Ti−Fe interaction is not yet fully determined. Furthermore, although not highlighted by the authors of ref 22, the K pre-edge of Fe^{2+} shows nonlocal features, occurring between the pre-edge transitions and the main edge. Unfortunately the data is measured in total fluorescence yield (TFY), yielding broad features, which are difficult to interpret. $K\alpha$ RIXS (1s2pRIXS) is a powerful technique to overcome this limitation as it enables effective suppression of the core−hole lifetime broadening.[23,24] This has already been demonstrated in the case of iron oxides and molecules, for which 1s2pRIXS provided new insights into the valence and spin states and orbital hybridization.[20,25,26]

Here we present the first 1s2pRIXS study of $FeTiO_3$. The obtained HERFD-XANES (high energy resolution fluorescence detected X-ray absorption near edge structure) and RIXS two-dimensional maps reveal five pre-edge distinct features. Comparison of experimental data with crystal field multiplet calculations and DFT calculated projected-density of states (pDOS) allows us to decompose the electric dipole and quadrupole contributions and to determine the on-site and nonlocal orbital hybridization of the Fe orbitals in $FeTiO_3$. We show how the two-dimensional RIXS map is a powerful tool to discuss the nature of the pre-edge features and probe the delocalization of the Fe $3d$ electrons over the two metal centers.

■ MATERIALS AND METHODS

Samples. The ilmenite sample was a commercial synthetic black powder. The chemical composition and crystalline structure of the sample were characterized by XRD (Figure S1). The sample was finely ground and prepared as a pellet diluted in boron nitride down to a concentration of 1 wt % of Fe for the RIXS measurements. For comparison we also measured hematite Fe_2O_3, which is isostructural to $FeTiO_3$ but contains formally high-spin Fe^{3+} instead of high-spin Fe^{2+}.

RIXS measurements. The 1s2pRIXS measurements were performed at the wiggler end-station BL6−2 of the Stanford Synchrotron Radiation Lightsource (SSRL). The storage ring was operating in top-up mode with a electron current of 500 mA. The energy of the incident X-ray beam was selected using a liquid-nitrogen-cooled double-crystal monochromator Si(311) with an energy bandwidth of 0.2 eV at 7.1 keV. The incident energy was calibrated using a Fe foil and setting the energy position of the first inflection point of the K-edge to 7112.0 eV. The beamsize on the sample was 138 μm × 395 μm. Total fluorescence yield (TFY) absorption spectra were recorded using a Si photodiode. The emitted X-ray photons were collected and analyzed using a five-crystal spectrometer. We used the (440) reflection of spherically bent (R = 1 m) Ge crystal analyzers. The sample was oriented 45° to the incident X-ray beam. The scattering angle was 90° and the analyzed X-rays were collected using a Silicon Drift Detector in Rowland geometry.[27] The energy of the emitted X-rays was calibrated through a series of elastic peaks in the Fe $K\alpha$ energy range (6300−6450 eV). The combined instrumental energy bandwidth was 0.66 eV full-width half-maximum (fwhm). Measurements were performed at room temperature with a helium chamber to minimize the absorption of the scattered X-rays.

Calculations. *Density functional theory calculations.* First-principles calculations of XANES and density of states (DOS) were performed using WIEN2k package based on linearized augmented plane-wave method within density functional theory.[28] We used the generalized gradient approximation (GGA) for the exchange correlation functional with the parametrization of Perdew et al.[29] The electronic correlation of Fe $3d$ are treated by Hubbard interaction. No Hubbard interaction was used for the empty $3d$ bands of Ti. An energy cutoff of 7.0 eV was used for plane wave basis set. The unit cell parameters were set to the experimental values: a = 5.0875 Å, c = 14.0827 Å.[30] The magnetic order was set to the antiferromagnetic configuration, in which the Fe^{2+} spins are ferromagnetically aligned within a layer but antiferromagnetically coupled between layers in agreement with experimental evidence.[31] We included a core hole effect on one Fe atom and use the final state rule to calculate the K-edge XANES spectrum. A 1 × 1 × 2 hexagonal supercell of 60 atoms was used to minimize the interaction between the core holes. The Fe K-edge absorption cross section was calculated in the electric dipole (E1) approximation. Finally, in order to interpret the pre-edge features, the projected-DOS are calculated on the supercell containing the core hole, with a 7 × 15 × 4 Monkhorst−Pack k-points grid and a Gaussian broadening of 0.50 eV. The input files are given in the Supporting Information.

Crystal field multiplet calculations. The multielectronic interactions arising in the local excitations of the RIXS map of Fe^{2+} were calculated using the framework of crystal field multiplet theory (CFM), which is a multielectronic, semiempirical approach initially developed by Thole et al. in the framework established by Cowan and Butler.[32] In this approach one considers an isolated Fe^{2+} ion embedded in a crystal field potential. It takes into account all the $3d−3d$ and $1s−3d$ electronic Coulomb interactions, as well as the spin−orbit coupling ζ on every open shell of the absorbing atom. Each of these many-body states is described by a linear combination of Slater determinants. More details on the method can be found in other references.[17] Calculations were performed using the quantum many-body script language QUANTY,[33] based on second quantization and Lanczos recursion method to calculate Green functions,[34] thus avoiding the explicit calculation of the intermediate and final states. The RIXS cross-section was calculated using the Kramers-Heisenberg equation.[35] In a first step, only the electric quadrupole contribution to
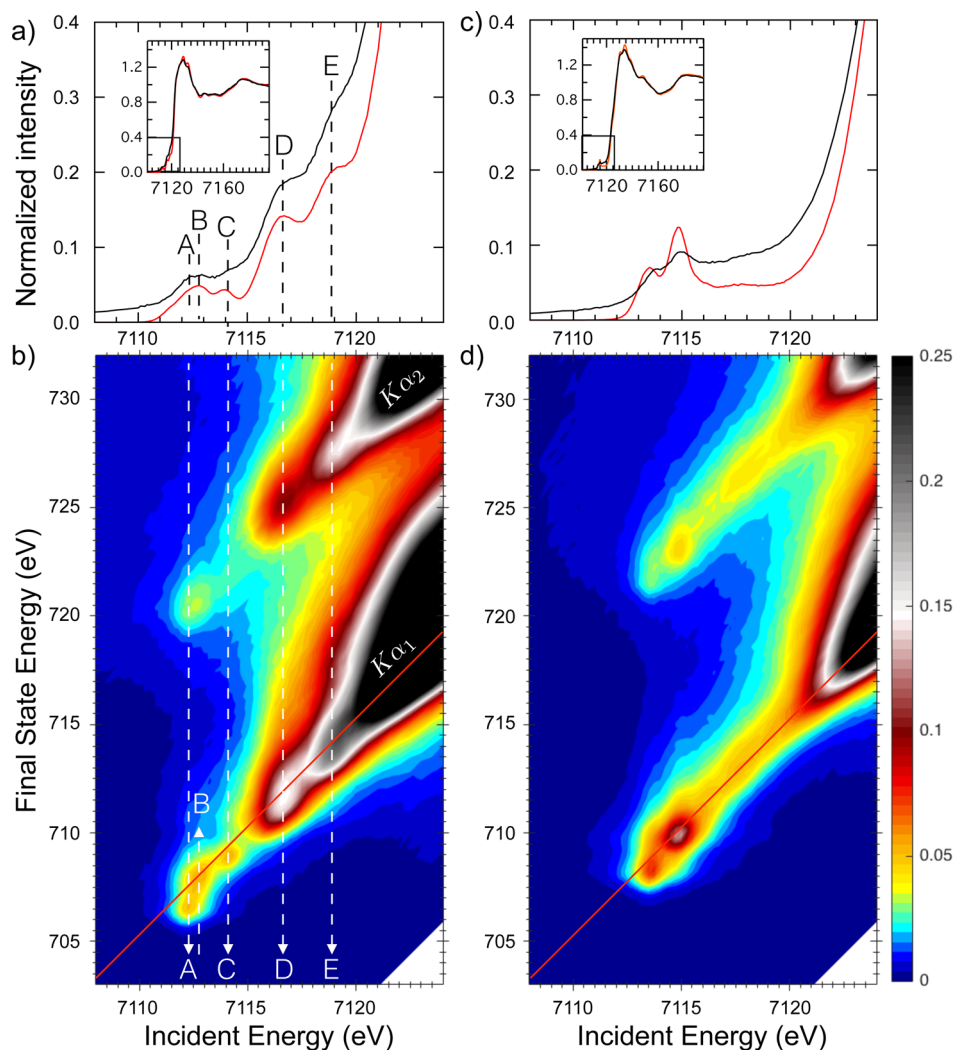
Figure 2. (a) Fe K-edge XANES spectra of $FeTiO_3$ in TFY detection compared with $K\alpha_1$-HERFD detection (red line). Inset: full energy range spectra. (b) 1s2pRIXS map of $FeTiO_3$ showing the five features labeled from (A) to (E). (c) TFY and HERFD spectra of Fe_2O_3. (d) 1s2pRIXS map of Fe_2O_3. The diagonal lines serve as guides for the eye to show the constant emitted energies for nonresonant $K\alpha_1$ emission (RIXS map color scale is the intensity normalized to the edge jump of the $K\alpha_1$-HERFD spectrum).

the absorption process of the RIXS was considered. To account for the Fe point group in $FeTiO_3$ we describe the crystal field in C_{3v} symmetry. Because the trigonal distortion is small compared to the energy resolution of RIXS, we use only the main crystal field parameter 10Dq set to 0.75 eV.[15] In first approximation, the multielectronic states will be described using the O_h point group irreps. The effect of bond covalency on the multielectronic interactions was described in the spherical approximation[36] by reducing homogeneously the Slater integrals by 64% of their Hartree–Fock value (corresponding to 80% of the atomic values). Spin–orbit coupling was kept to its Hartree–Fock calculated value.

The splitting of the lowest $^5T_{2g}$ (O_h) crystal-field term (ground state of the initial state of the RIXS) due to spin–orbit coupling was accounted using a Boltzmann weighting factor for each spectral contribution of the 15 microstates. Calculations were performed for T = 300 K. We note that at this temperature, the first three states represent c.a. 60% of the total contribution to the spectra. The natural core–hole lifetime and experimental broadenings are described respectively by a Lorentzian function and a Gaussian function (see details in the Supporting Information). We investigated the contribution of the electric dipole transitions to the pre-edge features of the RIXS process by considering on-site p-d mixing allowed in the approximated C_{3v} point group symmetry (as well as the real C_3 point group). This is achieved by following the method described by

Vercamer et al. and considering a hybridization Hamiltonian that depends on three mixing parameters in C_{3v} point group.[18] All the parameters used for these calculations (Table S1) and the input file for QUANTY are given in the Supporting Information.

■ RESULTS AND DISCUSSIONS

Experimental 1s2pRIXS results. The Fe K-edge HERFD-XANES spectrum measured using the maximum energy of the $K\alpha_1$ emission line (setting the RIXS spectrometer at 6404.7 eV) is compared to the TFY spectrum of $FeTiO_3$ in Figure 2a. The sharpening effect of the analyzer crystals becomes apparent mainly in the pre-edge region where several pre-edge features are more distinct in the HERFD-XANES spectrum than in the TFY spectrum. This is due to the effective reduction of the core–hole lifetime broadening obtained in RIXS.[23,24,37] The full RIXS map focuses on the pre-edge region (Figure 2b) and shows the intensity of the emitted X-rays plotted in energy transfer as a function of the incident energy. We observe both $K\alpha_1$ and $K\alpha_2$ emission lines corresponding to the decay channels $2p_{3/2} \rightarrow 1s$ and $2p_{1/2} \rightarrow 1s$, respectively. The HERFD-XANES spectrum in Figure 2a corresponds to a cut in the RIXS map along the diagonal red line plotted in Figure 2b, which
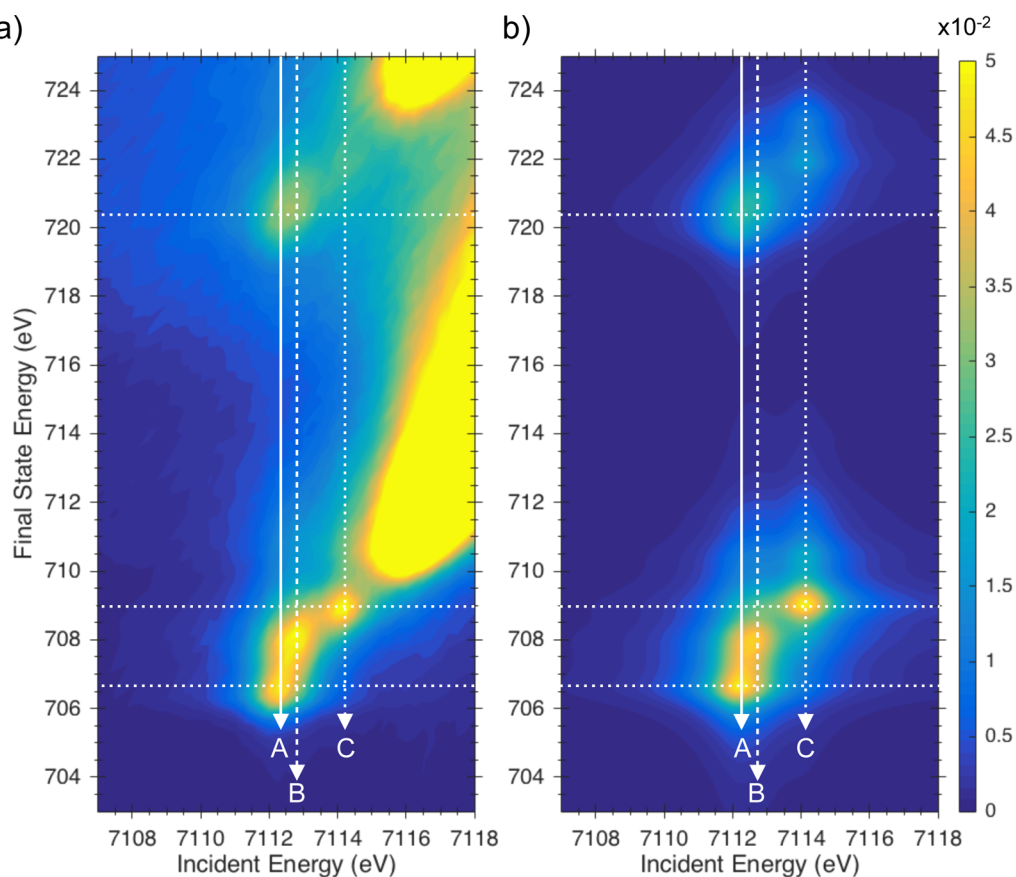
Figure 3. (a) Experimental 1s2pRIXS map of $FeTiO_3$ zoomed on features (A), (B), and (C). (b) Calculated 1s2pRIXS map of the local Fe^{2+} $1s \rightarrow 3d$ RIXS E2+E1 transitions.

corresponds to the constant emitted energy 6404.7 eV from the nonresonant $K\alpha_1$ emission.

The RIXS map of ilmenite shows in total five features in the $K\alpha_1$ emission direction, labeled from (A) to (E) (Figure 2b). Features (A), (B), and (C) in $FeTiO_3$ are spread both incident and emission energy-wise similarly to previously reported RIXS maps of 6-fold coordinated high-spin Fe^{2+} in siderite[38] and fayalite.[23] They can be assigned to the absorption transitions from the core−shell $1s$ to the $3d$ states of the absorbing Fe atom, followed by the resonant emission transitions to the final states with a $2p$ core−hole. The energy transfer positions of these three peaks are out-off the diagonal corresponding to the nonresonant $K\alpha_1$ emission (red line on Figure 2b). These peaks are assigned to the multielectronic final states and reflect the resonant emission process, which supports that the probed $3d$ states are localized on the absorbing Fe atom. Features (A), (B), and (C) are well separated from the edge rise due to the attraction by the $1s$ core−hole of the electron excited into the $3d$ orbitals.[23,38−40]

Figures 2c and 2d show the HERFD-XANES and the RIXS map of Fe^{3+} of the isostructural hematite Fe_2O_3 and are consistent with previous results.[20,26,41] The comparison with ilmenite shows that the main peak of the $3d$ resonances in the pre-edge of Fe^{3+} is observed at 7115 eV incident energy and 709 eV final state energy, which falls precisely between features (C) and (D) of the RIXS map of $FeTiO_3$. This supports previous conclusions that the oxidation state of Fe cations in ilmenite is Fe^{2+}.[15]

Approximately 4.5 eV above peak (A), the HERFD-XANES spectrum and the 1s2pRIXS map show two distinct features

(D) and (E) at the onset of the K-edge and separated by 2.5 eV. This confirms the presence of additional pre-edge features as suggested by previous K-edge TFY measurements[22] and highlights the advantage of HERFD-XANES and RIXS to identify peaks in the pre-edge otherwise buried in the rise of the Fe K-edge. Similar features have been observed in addition to the $1s \rightarrow 3d$ pre-edge excitations for other transition metal oxides. In the case of Fe^{3+} in hematite, the nonlocal features observed between 7116.5 and 7119 eV are assigned to electric dipole excitations into the delocalized $3d$ orbitals of the neighboring Fe, which contain some p character from the hybridization with the O $2p$ orbitals.[20] Nonlocal excitations have been reported for other transition metal cations in oxides such as Cr^{3+} in spinels,[42] Ti^{4+} in rutile,[21,43] Ni^{2+} in NiO,[44] and Co^{3+} in $LiCoO_3$.[45] Nonlocal features have also been observed in the Al K pre-edge in Fe:doped goethite and assigned to the Al^{3+} p states mixed with $3d$ states of the neighboring Fe^{3+}.[46] In these cases, the centrosymmetric point group (D_{2h} for Ti in rutile,[21] D_{3d} for Co in $LiCoO_3$,[45] and Cr in spinel[42]) was used as an argument to rule out significant hybridization between the local $3d$ and the $4p$ orbitals of the absorbing atom. As a consequence, these additional features were assigned to electric dipole transitions to the $4p$ states of the absorbing atom mixed with the $3d$ states of the neighboring atom. Thus, the "nonlocal" label means that the core-excited electron reaches delocalized states. More recently, HERFD-XANES results revealed nonlocal peaks in the Fe−Mo and Fe−V cluster.[12]

So far reported (HERFD-)XANES of high-spin Fe^{2+} in oxides, such as siderite or staurolite, did not show nonlocal features and ruled out the presence of delocalized Fe $4p$ bands

and strong orbital hybridization with neighboring atoms.[38,39] The present observation suggests that the corundum structure and the presence of neighboring Ti^{4+} ions may play a role. In particular, we can already note that the 2.5 eV energy splitting between features (D) and (E) matches the t_{2g}-e_g ligand field splitting reported for 6-fold coordinated Ti^{4+} in oxides such as rutile.[21,43] Here, by analogy with Fe_2O_3 and other previously reported cases, the observed peaks (D) and (E) may arise from electric dipole transitions to the delocalized Ti 3d orbitals, with some p character from hybribdization with O 2p and/or Fe 4p orbitals. To derive further information on the nature of the states involved in the five observed RIXS features, and confirm their assignment, we performed crystal field multiplet (CFM) and first-principle DFT calculations.

Crystal field multiplet analysis of the pre-edge features (A), (B), and (C). The semiempirical CFM model was used to account for multielectronic interactions in the calculation of the multiplet features (A), (B), and (C) arising in the 1s2pRIXS spectra of high-spin Fe^{2+} (Figure 3). We first describe the assignment of the multiplet features according to their energy and then we discuss the result of including the electric dipole (E1) contribution in the absorption process of the RIXS.

As shown in Figure 3, the energy positions of the calculated multiplet features match with the experimental ones (A), (B), and (C). The calculated energy positions in the incident energy direction depend mainly (see Supporting Information, Figure S2) on the Slater integrals describing the multieletronic interactions in the 3d shell of the $1s^1 3d^7$ electronic configuration of the RIXS intermediate state. The best match was obtained for a reduction of the Slater integrals to 64% of the values calculated by a Hartree–Fock method. This is 80% of the free ion values (80% of the Hartree–Fock calculated values) previously used for $L_{2,3}$-edge calculation of Fe^{2+} in $FeTiO_3$.[15] This reduction is interpreted as the nephelauxetic effect, due to the Fe–O chemical bonding and agrees with other CFM calculations of K-edge XANES for Fe^{2+} in oxides.[18,19] The incident energy positions of peaks (A), (B), and (C) do not vary significantly according to the incident energy resolution within ±20% of the crystal field parameter 10Dq set to 0.75 eV (see Figure S2).[15] As the energy positions of the peaks are well described within the experimental energy resolution by the crystal field parameter and Slater integrals reduction alone, we chose not to include the ligand field in order to minimize the number of parameters in the calculation.

The three observed features (A), (B), and (C) are assigned in Figure 4 to the absorption from the ground state $^5T_{2g}$ of the initial electronic configuration $1s^2 3d^6$ to the multiplet states $^5T_{1g}$, $^5T_{2g}$ (from the ^5F atomic term), and $^5T_{1g}$ (^5P) of the intermediate electronic configuration $1s^1 3d^7$ (labels given in O_h point group for simplicity). In the HERFD-XANES spectrum, only the tail of the first $^5T_{1g}$ (^5F) intermediate state is visible as a shoulder on the lower energy side. The $^5A_{2g}$ (^5F) crystal field term from the intermediate $1s^1 3d^7$ configuration cannot be reached by electric quadrupole absorption from the $^5T_{2g}$ RIXS initial state because of the orbital momentum selection rules. Furthermore, the spin-triplet states of the $1s^1 3d^7$ electronic configuration cannot be reached within strict the spin-selection rule $\Delta S = 0$.[47]

The experimental and calculated HERFD-XANES spectra (Figure 4) enable further comparison of the intensity of the features absorption-wise. The higher intensity of features (B) and (C) in the experimental HERFD-XANES spectrum
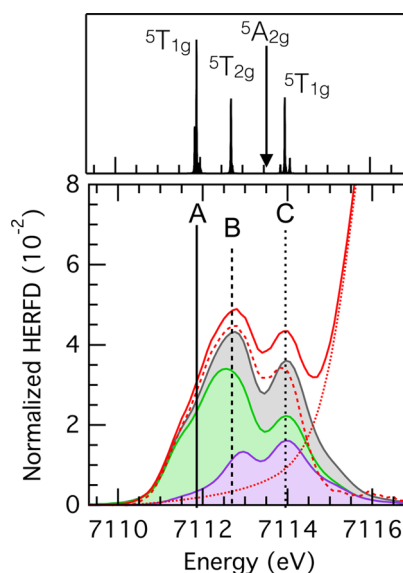

Figure 4. (Bottom) Calculated features (A), (B), and (C) of the Fe K-edge HERFD-XANES: E2 + E1 sum (black) and individual E2 (green) and E1 (violet) contributions compared to the experimental (red —) spectrum and the corrected (- - -) spectrum from the tail of feature (D) (···). (Top) Assignment of the $1s^1 3d^7$ multielectronic states (in O_h symmetry for simplicity).

compared to the calculated incident E2 contribution may arise from the tail of the nonlocal peak (D), which is partly supported by comparing with the tail-subtracted spectrum (see Figure S3 for further details on the fitting). It may also arise from an incident E1 absorption contribution to the RIXS signal. In a recent work, Vercamer et al. have estimated the influence of the site geometry and distortion on the relative contributions of electric quadrupole (E2) and electric dipole (E1) transitions to the absorption pre-edge of Fe^{2+}.[18] In the case of 6-fold coordinated sites, which only differ from a regular octahedron by small distortions, the E1 contribution to the pre-edge is weak but may affect the shape of the pre-edge. In ilmenite, the slightly higher intensity of peaks (B) and (C) may therefore also arise from local p-d mixing allowed by the trigonal distortion of the 6-fold coordinated Fe^{2+} site and the absence of inversion center in the point group of Fe (C_3).

The p-d hybridization Hamiltonian accounts for hybridization of d and p orbitals of the same symmetry (a_1 and e in C_{3v} approximated point group) via vibronic couplings within a given point group. In corundum, the A_1 vibration mode corresponds to the vibration along the c axis of the hexagonal unit cell. In order to estimate the dipole contribution to the local pre-edge, we have performed RIXS calculations including the local p-d hybridization with a_1 symmetry. For a mixing parameter $V_{pd}^{a_1} = 0.1\ eV$, the fraction of 4p electrons mixed with the 3d is ca. 1%. The individual HERFD-XANES spectra (Figure 4) and RIXS maps (Figure S4) of the incident E1 and E2 absorption contributions show that features (B) and (C) gain intensity from the E1 contribution. Overall, we estimate that the electric dipole absorption contribution to the pre-edge features (A), (B), and (C) represents 31% of the total pre-edge area integrated between 7110 and 7115 eV.

Figure 5 compares the experimental and calculated RIXS constant incident energy (CIE) spectra at (A), (B), and (C). The calculated CIE spectra account for both incident E1 and E2 contributions, and the detail of each is given in Figure S5.
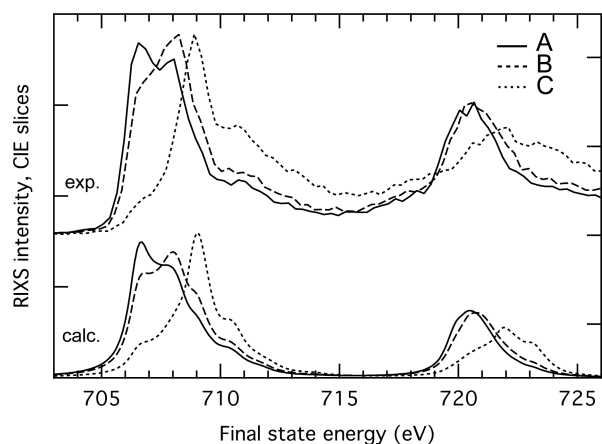
Figure 5. Experimental (top) and calculated (bottom) RIXS constant incident energy spectra obtained at (A), (B), and (C), corresponding to the white lines drawn in Figure 3.

Here again, we temporally use the approximated O_h point group and ignore the incident E1 contribution to describe the spectral features. The essential difference between the CIE spectra at (A) and (B) relates to the involved intermediate states ${}^5T_{1g}$ and ${}^5T_{2g}$, respectively. The CIE spectrum at (B) is close to the 2pXAS spectrum because the intermediate state in the RIXS has the same symmetry (${}^5T_{2g}$) as the initial state of the 2pXAS. In both 1s2pRIXS and 2pXAS cases, the electric dipole transition (emission for RIXS and absorption for XAS) brings the ${}^5T_{2g}$ intermediate state (initial state for 2pXAS) to the same final states from $2p^53d^7$. The decay of the intermediate state ${}^5T_{1g}$ (feature A) reaches final states of different symmetries, which explains the different spectral shape. Because the intermediate states of the RIXS features (A) and (C) are identical (${}^5T_{1g}$), the electric dipole emission will lead to exactly the same final states. However, different matrix elements result in different spectral shapes. The shift of the CIE spectrum at (C) in final state energy corresponds to the incident energy difference that is maintained in the decay process.[26] The small feature at 706.5 eV energy transfer in the CIE spectrum at (C) arises from the RIXS interference with the intermediate state of feature (A).

Altogether the CFM calculations support that the features (A), (B), and (C) arise from localized Fe* 3d states.

First-principle computed band-structure analysis of the nonlocal features (D) and (E). According to the parity selection rule, electric dipole K-edge absorption is restrained to $1s \rightarrow 4p$ transitions. To determine the origin of the E1 contribution to the pre-edge features (D) and (E) and to deduce the origin of the p character of the probed orbitals, we performed the DFT calculations of the density of states (DOS) of $FeTiO_3$ including the 1s core−hole on the absorbing Fe atom (herein after noted Fe*) and computed the electric dipole absorption cross section (Figure 6). As will be discussed below, the 1s core−hole mainly influences the Fe* 3d electrons; therefore, in Figure 6, the projected DOS (pDOS) of Fe* 4p, Fe 3d, Ti 3d, and 4p and O 2p show little change with the core−hole compared to the ground state system. The exact results of the calculations without core−hole are given in the Supporting Information (Figure S6).

The electronic structure of the ground state system (no core−hole) obtained with GGA-DFT and a Hubbard electronic correlation correction (U = 5 eV) is an insulator with a band
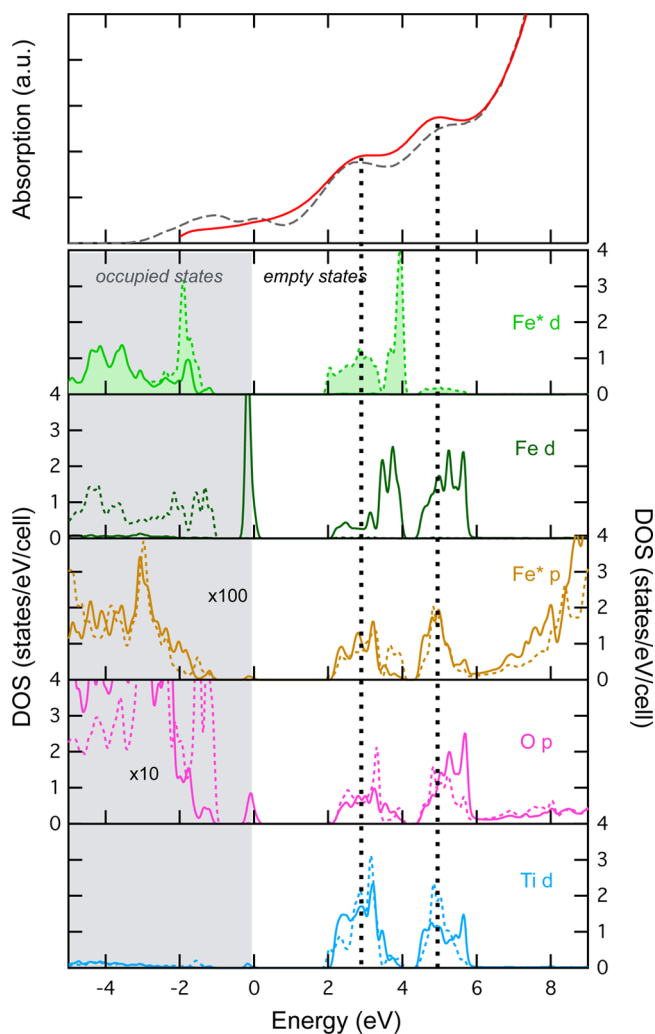

Figure 6. Calculated electric dipole absorption cross section (red plain line) at the Fe K-edge (top panel) compared with the projected DOS (lower panels) on Fe, Ti, and O (plain lines: β spin, dotted lines: α spin). The experimental HERFD-XANES is added for comparison (black dashed line, upper panel). Fe* denotes the Fe atom including the 1s core−hole.

gap of ca. 2 eV (Figure 6 and Figure S6). The calculated pDOS shows that the upper part of the valence band is composed of Fe 3d majority spin (α spin) states and the occupied Fe 3d minority spin (β spin) state mixed with the occupied O 2p states. These pDOS agree with the previously calculated ones.[22,48] The occupation of the 3d bands of Fe agrees with a high-spin Fe^{2+}: all α spin 3d bands are full; therefore, the spin state is high-spin (for low-spin electronic configuration, one would expect some empty α spin pDOS); the β spin 3d bands are partially filled; therefore, iron is in the divalent oxidation state (for high-spin Fe^{3+}, one would expect no electron in the β spin bands). This agrees with the interpretation of the features (A), (B), and (C) of the experimental 1s2pRIXS results.

Above the Fermi level, the bottom of the conduction band is split into two groups of bands centered around 3 and 5 eV. They correspond mainly to Fe 3d β spin and Ti 3d bands. The Fe and Ti 4p and O 2p pDOS also contribute. The relative energy position of the Fe and Ti 3d empty pDOS depends on the Hubbard U correction used for Fe atoms, while the relative energy positions of the other pDOS are not affected (Figure S6). The Ti 3d pDOS is separated into two main groups by ca.

2 eV, in agreement with the order of magnitude of the crystal field splitting of the 3d orbitals of Ti^{4+} in the 6-fold coordinated site.

Furthermore, in both the valence and conduction bands, the Fe and Ti 4p pDOS are mixed with the Fe and Ti 3d pDOS, respectively. This mixing may arise from the noncentrosymmetric point group of the metal ion sites.[18,19,47,49,50] It is noteworthy that the pDOS calculations reveal that the empty Fe* 3d states are also mixed with p states from Fe* and O. This supports the existence of an additional small E1 contribution to the features (A), (B), and (C) in the 1s2pRIXS. The Fe* 4p empty pDOS is 100 times smaller than the Fe* 3d empty pDOS at the same energies, in agreement with the fraction of p-character derived from the p-d mixing Hamiltonian used in the CFM calculations. The contribution from the pDOS from Fe 4p, Ti 4p, and O 2p in the two main energy ranges of the Ti 3d pDOS supports the hybridization between the delocalized Ti 3d orbitals with the neighboring O and Fe p orbitals.

When including the 1s core−hole (Figure 6), we observe that the Fe* 3d empty pDOS is the most affected and shifts down to lower energies. The pDOS of the neighboring Fe and Ti cations are almost unchanged, and the Fe* 4p and O 2p pDOS are only slightly influenced. The comparison between the relative energy positions of the occupied 3d pDOS of the Fe* and Fe reveals the energy shift of 2 eV induced by the 1s core−hole. The shift is similar to previously reported experimental trends of ca. 2.5 eV for Ti in rutile,[21] Cr spinels,[42] and Fe in hematite.[20] Although the electric quadrupole (E2) absorption to the Fe* 3d states was not calculated, the energy position of these states can be read from the pDOS. This energy is higher than the energy position of the E2 features (A), (B), and (C). This is a well understood limitation of the DFT GGA calculations, which overestimates the screening of the 1s core−hole. The capacity of alternative methods to better reproduce the 1s core−hole effect has been discussed in detail elsewhere and goes beyond the scope of the present paper.[21] Assuming a similar energy shift induced by the 1s core−hole on the Fe* 3d states of ilmenite, the empty 3d states of the nonexcited Fe should lie approximately 2.5 eV above the pre-edge features (A), (B), and (C), just before the nonlocal features. This is lower than the calculated position of the Fe 3d states and suggests that the energy of the Fe 3d empty pDOS is too high with GGA-U. However, the decrease of the Hubbard U would decrease the gap energy, in disagreement with the reported experimental gap of 2.75 eV. This shows that the electronic correlations are not fully accounted for by the GGA+U method.

As indicated by the two vertical black dotted lines in Figure 6, the calculated electric dipole (E1) XAS spectrum presents two features separated by ca. 2 eV. These two features before the main edge absorption agree with the experimental data. According to the pDOS, the central energy positions of these features match the two main empty pDOS of Ti 3d. The p character of the excited states probed by the E1 absorption results from the contributions of Fe* 4p, Ti 4p and O 2p. The electric quadrupole (E2) transitions to the neighboring Fe 3d states are expected to be negligible by analogy with other transition metal oxides.[21,42,44,45] These results confirm that the experimentally observed features (D) and (E) correspond to the E1 transitions to excited states of p character, which results from the hybridization between the neighboring Ti 3d delocalized orbitals and the Fe* 4p orbitals presumably via the O 2p orbitals.

Implications for photocatalysis. At the onset of the K-edge, the HERFD-XANES is a probe of the hybridization of the Fe* 3d and 4p orbitals via electric quadrupole and dipole absorption, respectively. Our experimental and theoretical results show that Fe* 3d and 4p states are mixed (features (A), (B), and (C)) and that Fe* 4p are mixed with delocalized Ti 3d states.

Thus, the features (D) and (E) are indirect probes of respectively the Ti 3d t_{2g} orbitals (oriented in between the Ti−O bonds) and e_g orbitals (oriented along the Ti−O bonds). In the present case, the trigonal distortion of the cation site induces the splitting of the e_g and t_{2g} orbitals into a_1 (z^2) and e (combination of xy, xz, xy and $x^2 - y^2$). Note that here, the z Cartesian axis is along one of the C_3 symmetry axes of the octahedron.[51] The projected DOS on the 3d orbitals of Fe (Figure S7) shows that the occupied β spin orbital is mainly the a_1 orbital (z^2). The projected DOS on the d orbitals of Ti is in agreement with previous calculations (Figure S7).[22] This leads to the a_1 orbital pointing through the Fe−Ti shared face as the occupied β spin orbital, in agreement with the measured polarization dependence of the MMCT optical (E1) absorption reported for (Fe−Ti):Al_2O_3 (blue sapphire) (ref 9c). Altogether, our results of the orbital projection of the 3d bands of the cations agree with the early molecular orbital calculation of Sherman[11] based on a $(FeTiO_{10})^{14-}$ edge-sharing cluster.

The two optical transitions to MMCT states are observed at 2.5 eV (500 nm) and 4.5 eV (275 nm) in optical spectroscopy[8] and Ti 2p3dRIXS.[16] In our DFT calculations, we find that the first Ti t_{2g} orbitals lie ca. 3 eV above the occupied β spin Fe 3d (t_{2g}) orbital and the Ti e_g orbitals lie ca. 5 eV above. Although these absolute energies are slightly higher than the energies of the excited MMCT states observed from experiment, their relative splitting in DFT and experimental 1s2pRIXS is in agreement with the splitting obtained in optical absorption spectroscopy. The Fe 4p/Ti 3d orbital hybridization demonstrated from our calculations supports that the electric dipole optical transitions to the MMCT states result from the Fe 4p character of these states. Previous O K-edge XAS results[22] have also confirmed the strong hybridization between O 2p and Ti 3d orbitals. Together with our DFT results, this supports that the Fe 4p/Ti 3d orbital hybridization is mediated via the O 2p orbitals. Since no such hybridization has been reported so far for divalent iron oxides, this highlights the particular role of Ti in the overlap between Fe and Ti orbitals, despite the localized Fe^{2+} 3d states. This hybridization is favorable for the electron mobility in ilmenite and supports its observed photocatalytical activity.

HERFD-XANES appears to be a powerful tool to probe the Fe−Ti orbital hybridization involved in MMCT, and the possibility to determine the mixing of the neighboring Ti states in the pre-edge of Fe K-edge will enable a better understanding of the role of Ti in the electronic structure of Ti-doped hematite. In particular, the microstructure of hematite thin films has been used to enhance the charge-carrier lifetime.[1a,1e1d] The influence of the preparation method and the crystallinity on the Fe−Ti orbital hybridization can thus be probed with the present approach, which benefits from the high penetration depth of hard X-rays and element selectivity combined with the high energy resolution provided by the HERFD-XANES.

In the case of mononuclear complexes, nonlocal peaks have been assigned to E1 transitions to antibonding π^* orbitals of the ligands (metal-to-ligand charge transfer states). Examples

were reported for manganese complexes[52] and ferrous low-spin model complex for cytochrome c.[25,53] For binuclear complexes, such as for the Fe—Ti complexes reported by Turlington et al.,[6d] the present results suggest that the investigation of nonlocal peaks via 1s2pRIXS should provide key insights into the orbital overlap between the two metal centers, the influence of the geometry of the linkage between the two metal sites and the influence of the nature of the bridging ligands. Recently, Rees et al. have used a similar approach to compare the iron—heterometal bonds in nitrogenase enzymes (Fe—Mo and Fe—V) and assigned nonlocal peaks in the HERFD-XANES at Fe K-edge to MMCT peak.[12]

Finally, these results open new perspectives for pump—probed experiments to investigate MMCT, with a specific focus on these nonlocal states at the Fe K-edge. Continuous laser excitation would enable localization of the optically excited photoelectron in steady state measurements as previously demonstrated for Au-TiO$_2$.[54] Time-resolved experiments as available at synchrotrons (picosecond time scale) or X-ray free electron lasers (femtosecond time scale)[55] would enable determination of the excitation and decay lifetimes of the metal-to-metal charge transfer excited states.

CONCLUSION

We report the first 1s2pRIXS results at the Fe K-edge of ilmenite, a model compound for MMCT, and the analysis of five pre-edge spectral features. The three first well distinct RIXS features are assigned mainly to electric quadrupole transitions to the localized Fe* 3d states, shifted to lower energy by the 1s core—hole. CFM calculations of these features confirm the dominating presence of Fe^{2+}. The small contribution of electric dipole absorption due to local *p-d* mixing allowed by the trigonal distortion of the cation site is supported by DFT and CFM calculations. Two other nonlocal features are assigned to electric dipole transitions to excited Fe* 4p states mixed with the neighboring Ti 3d states. The comparison with calculations enables demonstration that MMCT in ilmenite is favored by the hybridization between the Fe 4p and Ti 3d orbitals via the O 2p orbitals. This work demonstrates the importance of the pre-edge energy region of the transition metal K-edge where E1 and E2 transitions have equivalent intensities to probe the orbital hybridization between Fe and Ti in materials for photochemistry. It would be appealing in the next steps to use 1s2pRIXS to study the effect of Ti-doping in hematite in real photocatalyst systems. Furthermore, the better understanding of the Fe K-edge provides the basis for future time-resolved spectroscopic investigations of the lifetime of MMCT excited states.

ASSOCIATED CONTENT

S **Supporting Information**

The Supporting Information is available free of charge on the ACS Publications website at DOI: 10.1021/acs.inorgchem.7b00938.

> Sample characterization data. Crystal field multiplet calculation parameters. Fit of the pre-edge. Individual E1 and E2 contributions to the calculated RIXS maps and CIE spectra. Effect of the Hubbard U parameter on the calculated DOS (PDF)
>
> Input files for QUANTY and WIEN2k calculations (ZIP)

AUTHOR INFORMATION

Corresponding Authors
*E-mail: myrtille.hunault@synchrotron-soleil.fr.
*E-mail: f.m.f.degroot@uu.nl.

ORCID
Myrtille O. J. Y. Hunault: 0000-0002-3754-8630
Frank M. F. de Groot: 0000-0002-1340-2186

Notes
The authors declare no competing financial interest.

REFERENCES

(1) (a) Sivula, K.; Le Formal, F.; Grätzel, M. Solar Water Splitting: Progress Using Hematite (α-Fe$_2$O$_3$) Photoelectrodes. *ChemSusChem* **2011**, *4*, 432−449. (b) Katz, M. J.; Riha, S. C.; Jeong, N. C.; Martinson, A. B. F.; Farha, O. K.; Hupp, J. T. Toward solar fuels: Water splitting with sunlight and "rust"? *Coord. Chem. Rev.* **2012**, *256*, 2521−2529. (c) Prévot, M. S.; Sivula, K. Photoelectrochemical Tandem Cells for Solar Water Splitting. *J. Phys. Chem. C* **2013**, *117*, 17879−17893. (d) Le Formal, F.; Pendlebury, S. R.; Cornuz, M.; Tilley, S. D.; Grätzel, M.; Durrant, J. R. Back Electron−Hole Recombination in Hematite Photoanodes for Water Splitting. *J. Am. Chem. Soc.* **2014**, *136*, 2564−2574. (e) Bassi, P. S.; Gurudayal; Wong, L. H.; Barber, J. Iron based photoanodes for solar fuel production. *Phys. Chem. Chem. Phys.* **2014**, *16*, 11834. (f) Tamirat, A. G.; Rick, J.; Dubale, A. A.; Su, W.-N.; Hwang, B.-J. Using hematite for photoelectrochemical water splitting: a review of current progress and challenges. *Nanoscale Horiz.* **2016**, *1*, 243−267.

(2) (a) Ranjit, K. T.; Viswanathan, B. Synthesis, characterization and photocatalytic properties of iron-doped TiO$_2$ catalysts. *J. Photochem. Photobiol., A* **1997**, *108*, 79−84. (b) Pal, B.; Hata, T.; Goto, K.; Nogami, G. Photocatalytic degradation of o-cresol sensitized by iron−titania binary photocatalysts. *J. Mol. Catal. A: Chem.* **2001**, *169*, 147−155. (c) Droubay, T.; Rosso, K. M.; Heald, S. M.; McCready, D. E.; Wang, C. M.; Chambers, S. A. Structure, magnetism, and conductivity in epitaxial Ti -doped α-Fe$_2$O$_3$ hematite: Experiment and density functional theory calculations. *Phys. Rev. B: Condens. Matter Mater. Phys.* **2007**, *75*, DOI: 10.1103/PhysRevB.75.104412. (d) Kumari, S.; Singh, A. P.; Sonal; Deva, D.; Shrivastav, R.; Dass, S.; Satsangi, V. R. Spray pyrolytically deposited nanoporous Ti^{4+} doped hematite thin

films for efficient photoelectrochemical splitting of water. *Int. J. Hydrogen Energy* **2010**, *35*, 3985−3990. (e) Zhang, P.; Kleiman-Shwarsctein, A.; Hu, Y.-S.; Lefton, J.; Sharma, S.; Forman, A. J.; McFarland, E. Oriented Ti doped hematite thin film as active photoanodes synthesized by facile APCVD. *Energy Environ. Sci.* **2011**, *4*, 1020. (f) Zhao, B.; Kaspar, T. C.; Droubay, T. C.; McCloy, J.; Bowden, M. E.; Shutthanandan, V.; Heald, S. M.; Chambers, S. A. Electrical transport properties of Ti-doped Fe₂O₃ (0001) epitaxial films. *Phys. Rev. B: Condens. Matter Mater. Phys.* **2011**, *84*, DOI: [10.1103/PhysRevB.84.245325](). (g) Liao, P.; Carter, E. A. Hole transport in pure and doped hematite. *J. Appl. Phys.* **2012**, *112*, 013701. (h) Lian, X.; Yang, X.; Liu, S.; Xu, Y.; Jiang, C.; Chen, J.; Wang, R. Enhanced photoelectrochemical performance of Ti-doped hematite thin films prepared by the sol−gel method. *Appl. Surf. Sci.* **2012**, *258*, 2307−2311. (i) Zandi, O.; Klahr, B. M.; Hamann, T. W. Highly photoactive Ti-doped α-Fe₂O₃ thin film electrodes: resurrection of the dead layer. *Energy Environ. Sci.* **2013**, *6*, 634−642. (j) Fu, Z.; Jiang, T.; Liu, Z.; Wang, D.; Wang, L.; Xie, T. Highly photoactive Ti-doped α-Fe₂O₃ nanorod arrays photoanode prepared by a hydrothermal method for photoelectrochemical water splitting. *Electrochim. Acta* **2014**, *129*, 358−363. (k) Pu, A.; Deng, J.; Li, M.; Gao, J.; Zhang, H.; Hao, Y.; Zhong, J.; Sun, X. Coupling Ti-doping and oxygen vacancies in hematite nanostructures for solar water oxidation with high efficiency. *J. Mater. Chem. A* **2014**, *2*, 2491−2497. (l) Andriamiadamanana, C.; Laberty-Robert, C.; Sougrati, M. T.; Casale, S.; Davoisne, C.; Patra, S.; Sauvage, F. Room-Temperature Synthesis of Iron-Doped Anatase TiO₂ for Lithium-Ion Batteries and Photocatalysis. *Inorg. Chem.* **2014**, *53*, 10129−10139. (m) Zeng, Y.; Han, Y.; Zhao, Y.; Zeng, Y.; Yu, M.; Liu, Y.; Tang, H.; Tong, Y.; Lu, X. Advanced Ti-Doped Fe₂O₃@PEDOT Core/Shell Anode for High-Energy Asymmetric Supercapacitors. *Adv. Energy Mater.* **2015**, *5*, 1402176. (n) Toussaint, C.; le Tran, H. L.; Colson, P.; Dewalque, J.; Vertruyen, B.; Gilbert, B.; Nguyen, N. D.; Cloots, R.; Henrist, C. Combining Mesoporosity and Ti-Doping in Hematite Films for Water Splitting. *J. Phys. Chem. C* **2015**, *119*, 1642−1650. (o) Ren, H.; Koshy, P.; Cao, F.; Sorrell, C. C. Multivalence Charge Transfer in Doped and Codoped Photocatalytic TiO₂. *Inorg. Chem.* **2016**, *55*, 8071−8081.

(3) (a) Ginley, D. S.; Butler, M. A. The photoelectrolysis of water using iron titanate anodes. *J. Appl. Phys.* **1977**, *48*, 2019−2021. (b) Teoh, W. Y.; Amal, R.; Mädler, L.; Pratsinis, S. E. Flame sprayed visible light-active Fe-TiO₂ for photomineralisation of oxalic acid. *Catal. Today* **2007**, *120*, 203−213. (c) Rong, N.; Chu, M.; Tang, Y.; Zhang, C.; Cui, X.; He, H.; Zhang, Y.; Xiao, P. Improved photoelectrocatalytic properties of Ti-doped BiFeO₃ films for water oxidation. *J. Mater. Sci.* **2016**, *51*, 5712−5723. (d) García-Muñoz, P.; Pliego, G.; Zazo, J.; Bahamonde, A.; Casas, J. Ilmenite (FeTiO₃) as low cost catalyst for advanced oxidation processes. *J. Environ. Chem. Eng.* **2016**, *4*, 542−548. (e) Zarazúa-Morín, M. E.; Torres-Martínez, L. M.; Moctezuma, E.; Juárez-Ramírez, I.; Zermeño, B. B. Synthesis, characterization, and catalytic activity of FeTiO₃/TiO₂ for photo-degradation of organic pollutants with visible light. *Res. Chem. Intermed.* **2016**, *42*, 1029−1043.

(4) (a) Cordischi, D.; Burriesci, N.; D'Alba, F.; Petrera, M.; Polizzotti, G.; Schiavello, M. Structural characterization of Fe/Ti oxide photocatalysts by X-ray, ESR, and Mössbauer methods. *J. Solid State Chem.* **1985**, *56*, 182−190. (b) Gao, B.; Kim, Y. J.; Chakraborty, A. K.; Lee, W. I. Efficient decomposition of organic compounds with FeTiO₃/TiO₂ heterojunction under visible light irradiation. *Appl. Catal., B* **2008**, *83*, 202−207. (c) Kim, Y. J.; Gao, B.; Han, S. Y.; Jung, M. H.; Chakraborty, A. K.; Ko, T.; Lee, C.; Lee, W. I. Heterojunction of FeTiO₃ Nanodisc and TiO₂ Nanoparticle for a Novel Visible Light Photocatalyst. *J. Phys. Chem. C* **2009**, *113*, 19179−19184. (d) Truong, Q. D.; Liu, J.-Y.; Chung, C.-C.; Ling, Y.-C. Photocatalytic reduction of CO₂ on FeTiO₃/TiO₂ photocatalyst. *Catal. Commun.* **2012**, *19*, 85−89. (e) Liu, Q.; et al. Aligned Fe₂TiO₅-containing nanotube arrays with low onset potential for visible-light water oxidation. *Nat. Commun.* **2014**, *5*, 5122. (f) Li, X.; Bassi, P. S.; Boix, P. P.; Fang, Y.; Wong, L. H. Revealing the Role of TiO₂ Surface Treatment of Hematite Nanorods Photoanodes for Solar Water Splitting. *ACS Appl. Mater. Interfaces*

2015, *7*, 16960−16966. (g) Wang, M.; Pyeon, M.; Gönüllü, Y.; Kaouk, A.; Shen, S.; Guo, L.; Mathur, S. Constructing Fe₂O₃/TiO₂ core−shell photoelectrodes for efficient photoelectrochemical water splitting. *Nanoscale* **2015**, *7*, 10094−10100.

(5) (a) Vrachnou, E.; Vlachopoulos, N.; Grätzel, M. Efficient visible light sensitization of TiO₂ by surface complexation with Fe(CN)₆⁴⁻. *J. Chem. Soc., Chem. Commun.* **1987**, 868−870. (b) Ghosh, H. N.; Asbury, J. B.; Weng, Y.; Lian, T. Interfacial Electron Transfer between Fe(II)(CN)₆⁴⁻ and TiO₂ Nanoparticles: Direct Electron Injection and Nonexponential Recombination. *J. Phys. Chem. B* **1998**, *102*, 10208−10215. (c) Khoudiakov, M.; Parise, A. R.; Brunschwig, B. S. Interfacial Electron Transfer in FeII(CN)₆⁴⁻ Sensitized TiO₂ Nanoparticles: A Study of Direct Charge Injection by Electroabsorption Spectroscopy. *J. Am. Chem. Soc.* **2003**, *125*, 4637−4642. (d) Szacilowski, K.; Macyk, W.; Hebda, M.; Stochel, G. Redox-Controlled Photosensitization of Nanocrystalline Titanium Dioxide. *ChemPhysChem* **2006**, *7*, 2384−2391.

(6) (a) Curtis, J. C.; Meyer, T. J. Outer-sphere charge transfer in mixed-metal ion pairs. *Inorg. Chem.* **1982**, *21*, 1562−1571. (b) Yang, C.-H.; Ladd, J. A.; Goedken, V. L. New Heterobinuclear μ-Oxo-Bridged Dimer Complexes: Synthesis, Characterization and Structural Studies of a Macrocyclic Titanyl Complex and its Adducts. *J. Coord. Chem.* **1988**, *19*, 235−251. (c) Okamoto, A.; Nakamura, R.; Osawa, H.; Hashimoto, K. Site-Specific Synthesis of Oxo-Bridged Mixed-Valence Binuclear Complexes on Mesoporous Silica. *Langmuir* **2008**, *24*, 7011−7017. (d) Turlington, M. D.; Pienkos, J. A.; Carlton, E. S.; Wroblewski, K. N.; Myers, A. R.; Trindle, C. O.; Altun, Z.; Rack, J. J.; Wagenknecht, P. S. Complexes with Tunable Intramolecular Ferrocene to Ti^{IV} Electronic Transitions: Models for Solid State Fe^{II} to Ti^{IV} Charge Transfer. *Inorg. Chem.* **2016**, *55*, 2200−2211.

(7) (a) Blasse, G. *Complex Chemistry*; Springer, 1991; pp 153−187. (b) D'Alessandro, D. M.; Keene, F. R. Current trends and future challenges in the experimental, theoretical and computational analysis of intervalence charge transfer (IVCT) transitions. *Chem. Soc. Rev.* **2006**, DOI: 10.1039/b514590m. (c) Endicott, J. F.; Chen, Y.-J. Electronic coupling between metal ions in cyanide-bridged ground state and excited state mixed valence complexes. *Coord. Chem. Rev.* **2013**, *257*, 1676−1698.

(8) Strens, R. G. J.; Wood, B. J. Diffuse reflectance spectra and optical properties of some iron and titanium oxides and oxyhydroxides. *Mineral. Mag.* **1979**, *43*, 347−354.

(9) (a) Ferguson, J.; Fielding, P. E. The origins of the colours of natural yellow, blue, and green sapphires. *Aust. J. Chem.* **1972**, *25*, 1371−1385. (b) Eigenmann, K.; Günthard, H. H. Valence states, redox reactions and biparticle formation of Fe and Ti doped sapphire. *Chem. Phys. Lett.* **1972**, *13*, 58−61. (c) Townsend, M. G. Visible charge transfer band in blue sapphire. *Solid State Commun.* **1968**, *6*, 81−83.

(10) Goodenough, J. B. Direct Cation- -Cation Interactions in Several Oxides. *Phys. Rev.* **1960**, *117*, 1442−1451.

(11) Sherman, D. M. Molecular orbital (SCF-Xα-SW) theory of metal-metal charge transfer processes in minerals. *Phys. Chem. Miner.* **1987**, *14*, 355−363.

(12) Rees, J. A.; Bjornsson, R.; Kowalska, J. K.; Lima, F. A.; Schlesier, J.; Sippel, D.; Weyhermüller, T.; Einsle, O.; A. Kovacs, J.; DeBeer, S. Comparative electronic structures of nitrogenase FeMoco and FeVco. *Dalton Transactions* **2017**, *46*, 2445−2455.

(13) (a) Seda, T.; Hearne, G. R. Pressure induced Fe²⁺+Ti⁴⁺ → Fe³⁺+Ti³⁺ intervalence charge transfer and the Fe³⁺/Fe²⁺ ratio in natural ilmenite (FeTiO₃) minerals. *J. Phys.: Condens. Matter* **2004**, *16*, 2707. (b) Wu, X.; Steinle-Neumann, G.; Narygina, O.; Kantor, I.; McCammon, C.; Pascarelli, S.; Aquilanti, G.; Prakapenka, V.; Dubrovinsky, L. Iron oxidation state of FeTiO₃ under high pressure. *Phys. Rev. B: Condens. Matter Mater. Phys.* **2009**, *79*, 094106.

(14) Butorin, S. M.; Guo, J.-H.; Magnuson, M.; Nordgren, J. Resonant inelastic soft-x-ray scattering from valence-band excitations in 3d⁰ compounds. *Phys. Rev. B: Condens. Matter Mater. Phys.* **1997**, *55*, 4242.

(15) Radtke, G.; Lazar, S.; Botton, G. A. High-resolution EELS investigation of the electronic structure of ilmenites. *Phys. Rev. B: Condens. Matter Mater. Phys.* **2006**, *74*, DOI: 10.1103/PhysRevB.74.155117.

(16) (a) Agui, A.; Uozumi, T.; Mizumaki, M.; Käämbre, T. Intermetallic charge transfer in FeTiO₃ probed by resonant inelastic soft x-ray scattering. *Phys. Rev. B: Condens. Matter Mater. Phys.* **2009**, *79*, DOI: 10.1103/PhysRevB.79.092402. (b) Agui, A.; Mizumaki, M.; Uozumi, T. Intermetallic charge transfer in MTiO₃ (M = Mn, Fe, Co, and Ni) by Ti 2p edge resonant inelastic X-ray scattering. *J. Electron Spectrosc. Relat. Phenom.* **2015**, *205*, 106−110.

(17) Groot, F. d.; Kotani, A. *Core level spectroscopy of solids*; CRC Press: Boca Raton, United States, 2008.

(18) Vercamer, V. Calculation of optical and K pre-edge absorption spectra for ferrous iron of distorted sites in oxide crystals. *Phys. Rev. B* **2016**, *94*, 245115.

(19) Arrio, M.-A.; Rossano, S.; Brouder, C.; Galoisy, L.; Calas, G. Calculation of multipole transitions at the Fe K pre-edge through p - d hybridization in the Ligand Field Multiplet model. *Europhys. Lett.* **2000**, *51*, 454−460.

(20) Glatzel, P.; Mirone, A.; Eeckhout, S. G.; Sikora, M.; Giuli, G. Orbital hybridization and spin polarization in the resonant 1s photoexcitations of α-Fe₂O₃. *Phys. Rev. B: Condens. Matter Mater. Phys.* **2008**, *77*, 10.1103/PhysRevB.77.115133.

(21) Cabaret, D.; Bordage, A.; Juhin, A.; Arfaoui, M.; Gaudry, E. First-principles calculations of X-ray absorption spectra at the K-edge of 3d transition metals: an electronic structure analysis of the pre-edge. *Phys. Chem. Chem. Phys.* **2010**, *12*, 5619.

(22) Chen, S. W.; Huang, M. J.; Lin, P. A.; Jeng, H. T.; Lee, J. M.; Haw, S. C.; Chen, S. A.; Lin, H. J.; Lu, K. T.; Chen, D. P.; Dou, S. X.; Wang, X. L.; Chen, J. M. Orbital structure of FeTiO₃ ilmenite investigated with polarization-dependent X-ray absorption spectroscopy and band structure calculations. *Appl. Phys. Lett.* **2013**, *102*, 042107.

(23) Glatzel, P.; Bergmann, U. High resolution 1s core hole X-ray spectroscopy in 3d transition metal complexes−electronic and structural information. *Coord. Chem. Rev.* **2005**, *249*, 65−95.

(24) Bauer, M. HERFD-XAS and valence-to-core-XES: new tools to push the limits in research with hard X-rays? *Phys. Chem. Chem. Phys.* **2014**, *16*, 13827−13837.

(25) Kroll, T.; Hadt, R. G.; Wilson, S. A.; Lundberg, M.; Yan, J. J.; Weng, T.-C.; Sokaras, D.; Alonso-Mori, R.; Casa, D.; Upton, M. H.; Hedman, B.; Hodgson, K. O.; Solomon, E. I. Resonant Inelastic X-ray Scattering on Ferrous and Ferric Bis-imidazole Porphyrin and Cytochrome *c*: Nature and Role of the Axial Methionine-Fe Bond. *J. Am. Chem. Soc.* **2014**, *136*, 18087−18099.

(26) de Groot, F. M. F.; Glatzel, P.; Bergmann, U.; van Aken, P. A.; Barrea, R. A.; Klemme, S.; Hävecker, M.; Knop-Gericke, A.; Heijboer, W. M.; Weckhuysen, B. M. 1s2p Resonant Inelastic X-ray Scattering of Iron Oxides. *J. Phys. Chem. B* **2005**, *109*, 20751−20762.

(27) Sokaras, D.; Weng, T.-C.; Nordlund, D.; Alonso-Mori, R.; Velikov, P.; Wenger, D.; Garachtchenko, A.; George, M.; Borzenets, V.; Johnson, B.; Rabedeau, T.; Bergmann, U. A seven-crystal Johann-type hard x-ray spectrometer at the Stanford Synchrotron Radiation Lightsource. *Rev. Sci. Instrum.* **2013**, *84*, 053102.

(28) Blaha, P.; Schwarz, K.; Madsen, G. K. H.; Kvasnicka, D.; Luitz, J. *WIEN2K, An Augmented Plane Wave + Local Orbitals Program for Calculating Crystal Properties*; Karlheinz Schwarz, Techn. Universität Wien, Austria, 2001.

(29) Perdew, J. P.; Burke, K.; Ernzerhof, M. Generalized Gradient Approximation Made Simple. *Phys. Rev. Lett.* **1996**, *77*, 3865−3868.

(30) Wechsler, B. A.; Prewitt, C. T. Crystal structure of ilmenite (FeTiO₃) at high temperature and at high pressure. *Am. Mineral.* **1984**, *69*, 176−185.

(31) (a) Goodenough, J. B.; Stickler, J. J. Theory of the Magnetic Properties of the Ilmenites MTiO₃. *Phys. Rev.* **1967**, *164*, 768−778. (b) McDonald, P. F.; Parasiris, A.; Pandey, R. K.; Gries, B. L.; Kirk, W. P. Paramagnetic resonance and susceptibility of ilmenite, FeTiO₃ crystal. *J. Appl. Phys.* **1991**, *69*, 1104−1106.

(32) (a) Cowan, R. D. *The Theory of Atomic Structure and Spectra*; University of California Press: Berkeley, United States, 1981. (b) Butler, P. H. *Point group symmetry applications: methods and tables*; Plenum Press: New York, United States, 1981. (c) Thole, B. T.; Cowan, R. D.; Sawatzky, G. A.; Fink, J.; Fuggle, J. C. New probe for the ground-state electronic structure of narrow-band and impurity systems. *Phys. Rev. B: Condens. Matter Mater. Phys.* **1985**, *31*, 6856−6858.

(33) Haverkort, M. W. Quanty for core level spectroscopy - excitons, resonances and band excitations in time and frequency domain. *J. Phys.: Conf. Ser.* **2016**, *712*, 012001.

(34) Taillefumier, M.; Cabaret, D.; Flank, A.-M.; Mauri, F. X-ray absorption near-edge structure calculations with the pseudopotentials: Application to the K edge in diamond and α-quartz. *Phys. Rev. B: Condens. Matter Mater. Phys.* **2002**, *66*, DOI: 10.1103/PhysRevB.66.195107.

(35) Ament, L. J. P.; van Veenendaal, M.; Devereaux, T. P.; Hill, J. P.; van den Brink, J. Resonant inelastic x-ray scattering studies of elementary excitations. *Rev. Mod. Phys.* **2011**, *83*, 705−767.

(36) Schmidtke, H.-H. In *Optical Spectra and Chemical Bonding in Inorganic Compounds*; Mingos, D. M. P., Schönherr, T., Eds.; Structure and Bonding 106; Springer: Berlin Heidelberg, 2004; pp 19−35, DOI: 10.1007/b11303.

(37) Rueff, J. P.; Shukla, A. A RIXS cookbook: Five recipes for successful RIXS applications. *J. Electron Spectrosc. Relat. Phenom.* **2013**, *188*, 10−16.

(38) Rueff, J.-P.; Journel, L.; Petit, P.-E.; Farges, F. Fe K pre-edges as revealed by resonant x-ray emission. *Phys. Rev. B: Condens. Matter Mater. Phys.* **2004**, *69*, 235107.

(39) Wilke, M.; Farges, F.; Petit, P.-E.; Brown, G. E.; Martin, F. Oxidation state and coordination of Fe in minerals: An Fe K-XANES spectroscopic study. *Am. Mineral.* **2001**, *86*, 714−730.

(40) Galoisy, L.; Calas, G.; Arrio, M.-A. High-resolution XANES spectra of iron in minerals and glasses: structural information from the pre-edge region. *Chem. Geol.* **2001**, *174*, 307−319.

(41) Caliebe, W. A.; Kao, C.-C.; Hastings, J. B.; Taguchi, M.; Kotani, A.; Uozumi, T.; de Groot, F. M. F. 1s2p resonant inelastic x-ray scattering in α-Fe₂O₃. *Phys. Rev. B: Condens. Matter Mater. Phys.* **1998**, *58*, 13452−13458.

(42) Verger, L.; Dargaud, O.; Rousse, G.; Rozsályi, E.; Juhin, A.; Cabaret, D.; Cotte, M.; Glatzel, P.; Cormier, L. Spectroscopic properties of Cr³⁺ in the spinel solid solution ZnAl₂₋ₓCrₓO₄. *Phys. Chem. Miner.* **2016**, *43*, 33.

(43) Kas, J.; Rehr, J.; Tromp, M.; Thomas, R. J.; Glatzel, P. Real Space Green's Function Approach to Resonant Inelastic X-Ray Scattering and HERFD XAS. *J. Phys.: Conf. Ser.* **2013**, *430*, 012003.

(44) Gougoussis, C.; Calandra, M.; Seitsonen, A.; Brouder, C.; Shukla, A.; Mauri, F. Intrinsic charge transfer gap in NiO from Ni K-edge x-ray absorption spectroscopy. *Phys. Rev. B: Condens. Matter Mater. Phys.* **2009**, *79*, 10.1103/PhysRevB.79.045118.

(45) Juhin, A.; de Groot, F.; Vankó, G.; Calandra, M.; Brouder, C. Angular dependence of core hole screening in LiCoO₂: A DFT+U calculation of the oxygen and cobalt K-edge x-ray absorption spectra. *Phys. Rev. B: Condens. Matter Mater. Phys.* **2010**, *81*, 115115.

(46) Ducher, M.; Blanchard, M.; Vantelon, D.; Nemausat, R.; Cabaret, D. Probing the local environment of substitutional Al³⁺ in goethite using X-ray absorption spectroscopy and first-principles calculations. *Phys. Chem. Miner.* **2016**, *43*, 217.

(47) Westre, T. E.; Kennepohl, P.; DeWitt, J. G.; Hedman, B.; Hodgson, K. O.; Solomon, E. I. A Multiplet Analysis of Fe K-Edge 1s → 3d Pre-Edge Features of Iron Complexes. *J. Am. Chem. Soc.* **1997**, *119*, 6297−6314.

(48) Wilson, N. C.; Muscat, J.; Mkhonto, D.; Ngoepe, P. E.; Harrison, N. M. Structure and properties of ilmenite from first principles. *Phys. Rev. B: Condens. Matter Mater. Phys.* **2005**, *71*, 71.

(49) de Groot, F.; Vankó, G.; Glatzel, P. The 1s x-ray absorption pre-edge structures in transition metal oxides. *J. Phys.: Condens. Matter* **2009**, *21*, 104207.

(50) Bordage, A.; Balan, E.; Villiers, J. P. R.; Cromarty, R.; Juhin, A.; Carvallo, C.; Calas, G.; Sunder Raju, P. V.; Glatzel, P. V oxidation state in Fe−Ti oxides by high-energy resolution fluorescence-detected X-ray absorption spectroscopy. *Phys. Chem. Miner.* **2011**, *38*, 449−458.

(51) In the C_3 point group, with the C_3 axis along the z direction, the usual cubic Cartesian orbitals are not eigenstates of the single electron crystal field Hamiltonian. A detailed solution is given in ref 18.

(52) Roemelt, M.; Beckwith, M. A.; Duboc, C.; Collomb, M.-N.; Neese, F.; DeBeer, S. Manganese K-Edge X-Ray Absorption Spectroscopy as a Probe of the Metal−Ligand Interactions in Coordination Compounds. *Inorg. Chem.* **2012**, *51*, 680−687.

(53) Lundberg, M.; Kroll, T.; DeBeer, S.; Bergmann, U.; Wilson, S. A.; Glatzel, P.; Nordlund, D.; Hedman, B.; Hodgson, K. O.; Solomon, E. I. Metal−Ligand Covalency of Iron Complexes from High-Resolution Resonant Inelastic X-ray Scattering. *J. Am. Chem. Soc.* **2013**, *135*, 17121−17134.

(54) Chen, L. X.; Shelby, M. L.; Lestrange, P. J.; Jackson, N. E.; Haldrup, K.; Mara, M. W.; Stickrath, A. B.; Zhu, D.; Lemke, H.; Chollet, M.; Hoffman, B. M.; Li, X. Imaging ultrafast excited state pathways in transition metal complexes by X-ray transient absorption and scattering using X-ray free electron laser source. *Faraday Discuss.* **2016**, *194*, 639−658.

(55) Santomauro, F. G.; et al. Femtosecond X-ray absorption study of electron localization in photoexcited anatase TiO_2. *Sci. Rep.* **2015**, *5*, 1483410.1038/srep14834.

(56) Momma, K.; Izumi, F. *VESTA3* for three-dimensional visualization of crystal, volumetric and morphology data. *J. Appl. Crystallogr.* **2011**, *44*, 1272−1276.